1820 Bull. Chem. Soc. Jpn. Vol. 79, No. 12, 1820–1833 (2006)

*Award Accounts*

**The Chemical Society of Japan Award for Creative Work for 2004**

# Tuning of Electronic Structures of Quasi-One-Dimensional Halogen-Bridged Ni–Pd Mixed-Metal Complexes, $[Ni_{1-x}Pd_x(chxn)_2X]X_2$ (X = Cl, Br) with Strong Electron Correlation

**Masahiro Yamashita*** **and Shinya Takaishi**

Department of Chemistry, Graduate School of Science, Tohoku University & CREST(JST),
Aramaki-Aza-Aoba, Aoba-ku, Sendai 980-8578

Received May 10, 2006; E-mail: yamasita@agnus.chem.tohoku.ac.jp

This article describes the tuning of the electronic structures in a series of quasi-one-dimensional halogen-bridged Ni–Pd mixed-metal complexes, $[Ni_{1-x}Pd_x(chxn)_2X]X_2$ (chxn = 1*R*,2*R*-diaminocyclohexane; X, Y = Cl or Br). In these compounds, planar $[M(chxn)_2]$ units are bridged by halogen ions (X), forming linear chain M–X–M structures. Therefore, their electronic structures are 1D and are composed of hybridization between the $d_{z^2}$ orbitals of the metal ions and $p_z$ orbitals of the bridging halogens. In this system, electron-correlation on the Ni sites and electron–phonon interaction on the Pd sites should compete with each other. Their electronic structures have been investigated by means of the single-crystal reflectance, ESR and IR spectroscopies, electrical conductivities, and X-ray diffuse scattering. Moreover, their local electronic structures have been directly observed by scanning tunneling microscopy (STM) using single-crystals at room temperature and under ambient pressure. As a result, while the oxidation state of the Ni sites is +3 in all mixing ratios in these compounds due to strong electron-correlation, the conversion from the $Pd^{III}$ Mott–Hubbard states to the $Pd^{II}$–$Pd^{IV}$ mixed-valence states is observed around $x \approx 0.90$ for Br and $x \approx 0.85$ for Cl. Interestingly, the spin-soliton in $Ni_{0.05}Pd_{0.95}(chxn)_2Br_3$ was directly observed by STM for the first time.

## 1. Introduction

In one-dimensional (1D) electronic systems, very interesting physical properties are observed because of spin-charge-phonon coupling. Therefore, the quasi-1D compounds have attracted considerable attention due to their novel physical properties, such as the Peierls transition, spin-Peierls transition, neutral-ionic transition, charge density wave (CDW) states, spin density wave (SDW) states, Mott–Hubbard (MH) states, superconductivities, etc.[1] Amongst these compounds, quasi-1D halogen-bridged mixed-valence compounds (hereafter abbreviated as MX-chains) have been extensively investigated over the last 20 years, since they exhibit a wide range of interesting physical properties. These include intense and dichroic inter-valence charge-transfer (CT) bands, a progressive overtone in resonance Raman spectra, luminescence spectra with large Stokes-shifts, mid-gap absorptions attributable to solitons and polarons, large third-order nonlinear optical properties, 1D model compounds of high $T_c$ copper-oxide superconductors, etc.[2] The excited states and the relaxation process of these compounds have been investigated as a prototype material for 1D electronic systems by pico- and femto-second time-resolved optical methods.[3] The creation of solitons and polarons have been controlled by using the differences in their dimensionalities of the CDW states or hydrogen-bond networks.[4] The third-order nonlinear optical susceptibilities of these compounds are observed to be larger than that of poly-diacetylene or poly-silane.[5] Indeed, recently a gigantic third-order optical nonlinear susceptibility has been observed in $[Ni(chxn)_2Br]Br_2$ ($10^{-4}$ esu).[6]

From a theoretical viewpoint, the MX-chain compounds are regarded as Peierls–Hubbard system. In such a system, the electron–phonon interaction (S), the electron-transfer energy (T), the on-site and inter-site Coulomb interactions (U and V, respectively) compete and/or cooperate with one another (Fig. 1).[7] Originally, these MX-chain compounds were regarded to be in a 1D metallic state with half-filled $d_{z^2}$ orbitals of the metals and filled $p_z$ orbitals of the bridging halogens. However, it is well known that in these compounds the 1D metallic state is unstable and that the system subsequently changes to an insulating state via electron–phonon interaction (S) or electron correlation (U). In most MX-chain compounds, due to the strong electron–phonon interaction, the bridging halogens are displaced from the midpoints between two neighboring metal atoms, giving rise to CDW states or $M^{II}$–$M^{IV}$ mixed-valence states ($\cdots M^{II}\cdots X–M^{IV}–X\cdots M^{II}\cdots$) (Fig. 2a). Accordingly, the half-filled metallic band is split into an occupied valence band and an unoccupied conduction band with a finite Peierls gap. Therefore, these compounds belong to class II in the Robin–Day classification for the mixed-valence complexes.[8] The

Published on the web December 13, 2006; doi:10.1246/bcsj.79.1820

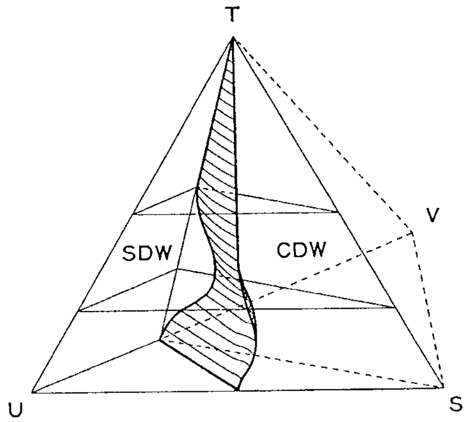

Fig. 1. S–T–U–V phase diagram of Peierls–Hubbard system.

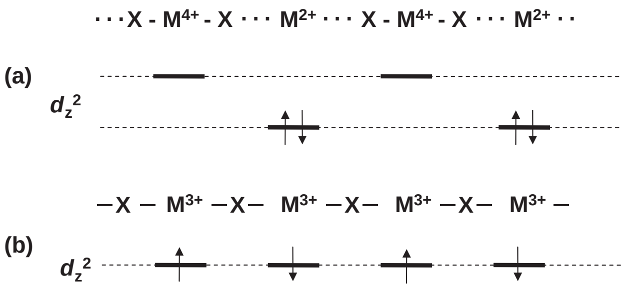

Fig. 2. Schematic structures: (a) CDW states or mixed-valence states for Pt and Pd, (b) Mott-insulator or charge-transfer insulator for Ni.

compounds are formulated as $[M^{II}(AA)_2][M^{IV}(AA)_2X_2]Y_4$ ($M^{II}$–$M^{IV}$ = $Pt^{II}$–$Pt^{IV}$, $Pd^{II}$–$Pd^{IV}$, $Ni^{II}$–$Pt^{IV}$, $Pd^{II}$–$Pt^{IV}$, and $Cu^{II}$–$Pt^{IV}$; X = Cl, Br, I, and mixed-halides; AA = ethylenediamine (en), 1*R*,2*R*-diaminocyclohexane (chxn), 2*R*,3*R*-butanediamine (bn), etc; Y = $ClO_4$, $BF_4$, X, etc.). These MX-chains have two characteristic features when compared with inorganic semiconductors and organic conjugated polymers: (1) the magnitudes of the band gaps or CDW strengths can be tuned by varying the chemical composition such as M, AA, X, and Y, in other words, the physical parameters (S, T, U, and V) can be tuned by substitution of various chemical factors and (2) the inter-chain interaction can be controlled via the intra- and inter-chain hydrogen-bond networks between the amino-hydrogens and counter-anions by substituting the counter-anions such as $ClO_4$ and X.[9]

Theoretically, it has been proposed that the $M^{III}$ state or MH state, where the bridging halogens are located at the midpoints between two neighboring metal ions (–X–$M^{III}$–X–$M^{III}$–X–), can be considered to be the more stable when there is a stronger U compared to S (Fig. 2b). Therefore, these compounds belong to class III in the Robin–Day classification for the mixed-valence complexes.[8] Our group has succeeded in synthesizing such compounds, formulated as $[Ni^{III}(chxn)_2X]Y_2$ (X = Cl, Br, or mixed-halides; Y = Cl, Br, mixed-halides, $ClO_4$, $BF_4$, or $NO_3$) for the first time. The choice of Ni is because the Ni ion has a stronger U than that of a Pd or Pt ion.[10] These $Ni^{III}$ compounds have a very strong antiferromagnetic interaction among spins located on $3d_{z^2}$ orbitals of each $Ni^{III}$ ion throughout the bridging halogens ($J \approx 2800\,K$). The X-ray photoelectron spectra (XPS), Auger spectra and single-crystal reflectance spectra have showed that, strictly speaking, these Ni compounds are not Mott insulators but CT insulators, where the energy levels of the bridging halogens are located between the upper- and lower-Hubbard bands composed of the $Ni^{III}$ $d_{z^2}$ orbitals. Therefore, the electronic structures of the Ni compounds are similar to those of the starting materials of the copper oxide superconductors, except for their dimensionality (Fig. 3). These $Ni^{III}$ compounds undergo a spin-Peierls transition below 100 K.[11]

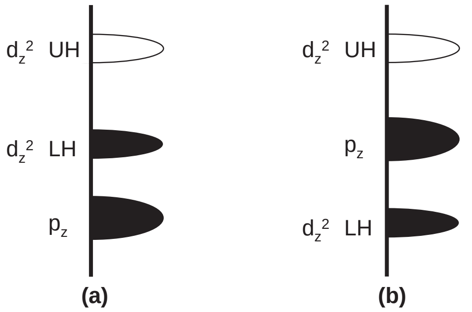

Fig. 3. Schematic electronic structures: (a) Mott-insulator, (b) charge-transfer insulator.

Simply speaking, for MX complexes with a stronger S, the oxidation states of the metal ions are the $M^{II}$–$M^{IV}$ (CDW states). On the other hand, in the case of a stronger U, the oxidation states are $M^{III}$ states (MH state or CT insulator state).

The $[Pd(chxn)_2][Pd(chxn)_2X_2]X_4$ and $[Ni(chxn)_2X]X_2$ are isomorphous to each other, although the bridging halogens are displaced from the midpoints in the former and centered between two neighboring Ni ions in the latter. More recently, we have succeeded in synthesizing a series of single-crystals of Ni–Pd mixed-metal compounds with the formula $[Ni_xPd_{1-x}(chxn)_2X]X_2$ (X = Cl and Br), where S on $Pd^{II}$–$Pd^{IV}$ sites (CDW states) and U on $Ni^{III}$ sites compete with each other. In this review, we will describe the tuning of the electronic structures in Ni–Pd mixed-metal compounds, $[Ni_{1-x}Pd_x(chxn)_2X]X_2$ (X = Cl and Br). Their electronic structures have been investigated by means of IR, ESR, reflectance spectra, electrical conductivities, X-ray diffuse scattering, and STM.

## 2. Experiments

Starting materials, $[Ni(chxn)_2]X_2$ and $[Pd(chxn)_2]X_2$ were synthesized by the methods previously reported.[12] Single-crystals of a series of Ni–Pd mixed-metal complexes were synthesized by electro-chemical oxidation methods of the methanol solutions of various ratios of the Ni and Pd starting materials $[M(chxn)_2]X_2$, including the tetrabutylammonium halides as an electrolyte. After a few weeks, the good quality single-crystals were obtained. Elemental analyses of the metal ions were carried out by using ICP methods. Physical measurements of these compounds were carried out by the conventional methods described elsewhere.[2,10]

## 3. Structures of $[Ni_{1-x}Pd_x(chxn)_2X]X_2$

The crystal structure of $[Ni^{III}(chxn)_2Br]Br_2$ is shown in Fig. 4a. In this structure, the $Ni^{III}$ ions and $Br^-$ ions are alternately arranged with equivalent Ni–Br distances, and the four N atoms of the two chxn ligands that are coordinated to a $Ni^{III}$

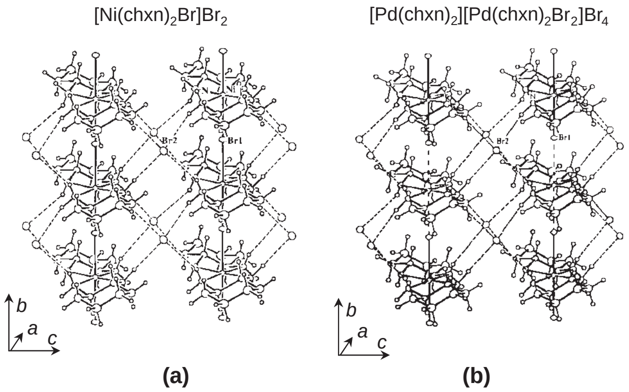

Fig. 4. Crystal structures of (a) [Ni$^{III}$(chxn)$_2$Br]Br$_2$ and (b) [Pd$^{II}$(chxn)$_2$][Pd$^{IV}$(chxn)$_2$Br$_2$]Br$_4$.

ion in equatorial positions produce a strong ligand field. Each Ni–Br–Ni chain is hydrogen-bonded between amino-hydrogens of chxn and counter Br ions along the chains as well as over the chains, forming two-dimensional hydrogen-bond networks. However, the electronic structure of this compound is still one-dimensional. The resultant electronic configuration of the Ni$^{III}$ ion is $(t_{2g})^6(e_g)^1$ with one unpaired electron in the $d_{z^2}$ orbital. The 1D electronic structure is composed of the hybridization between the Br $p_z$ orbitals and the Ni $d_{z^2}$ orbitals. The large U on the Ni sites ($U \approx 5\,\mathrm{eV}$) results in a large MH gap between Ni 3d upper Hubbard band and the lower Hubbard band. The Br $p_z$ band is located in this gap, such that the charge-transfer (CT) transition from the Br $p_z$ valence band to the Ni 3d upper-Hubbard band corresponds to the optical gap. Thus, correctly speaking, the Ni compound is a CT insulator as mentioned above. Unpaired electrons in the Ni $d_{z^2}$ orbitals form a 1D antiferromagnetic spin ($S = 1/2$) chain. The large p–d hybridization between the Br $p_z$ orbital and the Ni $d_{z^2}$ orbital leads to a large antiferromagnetic exchange interaction parameter $J$, which has been evaluated to be 2800 K. The crystal and electronic structures of [Ni(chxn)$_2$Cl]Cl$_2$ are essentially the same as those of [Ni(chxn)$_2$Br]Br$_2$.

The Pd$^{II}$–Pd$^{IV}$ mixed-valence compound, [Pd(chxn)$_2$][Pd(chxn)$_2$Br$_2$]Br$_4$ is isomorphous to the [Ni(chxn)$_2$Br]Br$_2$ except for the positions of the bridging Br$^-$ ions (Fig. 4b). In the Pd compound, the bridging Br$^-$ ions are displaced from the midpoints between two neighboring Pd ions due to both the strong S and the relatively small U between 4d electrons, stabilizing the Peierls-distorted state or the commensurate CDW state with alternating arrangements of Pd$^{II}$ and Pd$^{IV}$ units even at room temperature. Therefore, the Pd compound is diamagnetic. Intense inter-valence CT bands from Pd$^{II}$ sites to Pd$^{IV}$ sites are observed at around 0.75 eV. The crystal and electronic structures of [Pd(chxn)$_2$][Pd(chxn)$_2$Cl$_2$]Cl$_4$ are essentially the same as that of [Pd(chxn)$_2$][Pd(chxn)$_2$Br$_2$]Br$_4$.

X-ray powder patterns of [Ni$_{1-x}$Pd$_x$(chxn)$_2$X]X$_2$ were measured and are isomorphous to each other and to M(chxn)$_2$X$_3$ (M = Pd and Ni). Therefore, [Ni$_{1-x}$Pd$_x$(chxn)$_2$X]X$_2$ are supposed to have halogen-bridged linear chain structures composed of alternating stacks of [M(chxn)$_2$] and bridging halogens. Each chain is hydrogen-bonded along the chain as well as over the chains, forming two-dimensional hydrogen-bonding networks.

### 4. IR Spectra of [Ni$_{1-x}$Pd$_x$(chxn)$_2$X]X$_2$

Information on the valences ($\rho$) of the metal ions can be obtained from $\nu$(N–H) in the IR spectum, because the two-dimensional N–H···Br hydrogen bonds are strongly influenced by the oxidation states of the central metal ions. Okaniwa et al. investigated the relation between the oxidation states and the splitting of $\nu$(N–H) in [M(chxn)$_2$Br]Br$_2$ (M = Pt, Pd, and Ni) (Fig. 5).[13] In the Pt and Pd complexes, splitting of $\nu$(N–H) was observed because the metal ions are in a M$^{II}$–M$^{IV}$ mixed-valence state, that is, the different electron densities of N atoms in [M$^{II}$(chxn)$_2$]$^{2+}$ and [M$^{IV}$(chxn)$_2$X$_2$]$^{2+}$ units. On the other hand, the $\nu$(N–H) in [Ni(chxn)$_2$Br]Br$_2$ is not split, because the oxidation state of Ni ion is +3 basically. Interestingly, in the order of Pt, Pd, and Ni, the magnitudes of splitting of $\nu$(N–H) have a linear correlation against the magnitudes of the displacement of the bridging halogens and decrease in this

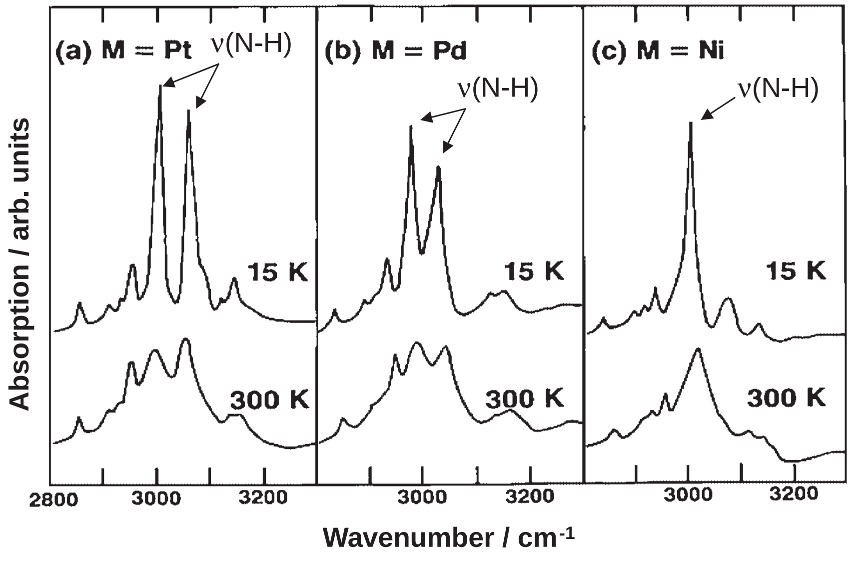

Fig. 5. IR spectra of [M(chxn)$_2$Br]Br$_2$ (M = Pt, Pd, and Ni) measured at 15 and 300 K.

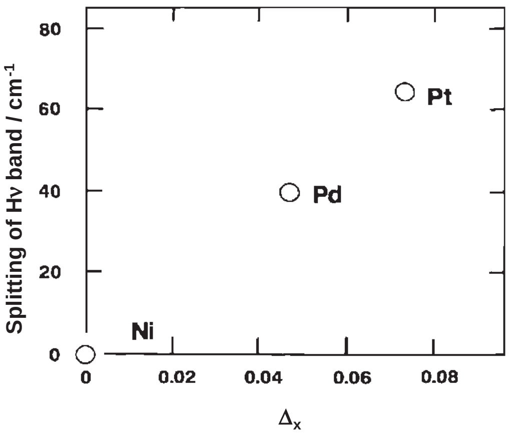

Fig. 6. Correlation between the splitting of H$\nu$ band the normalized halogen displacement from the midpoint between two metals, $\Delta_x = (l_1 - l_2)/(l_1 + l_2)$, where $l_1$ and $l_2$ are the distances $M^{II}\cdots X$ and $M^{IV}$–X, respectively.

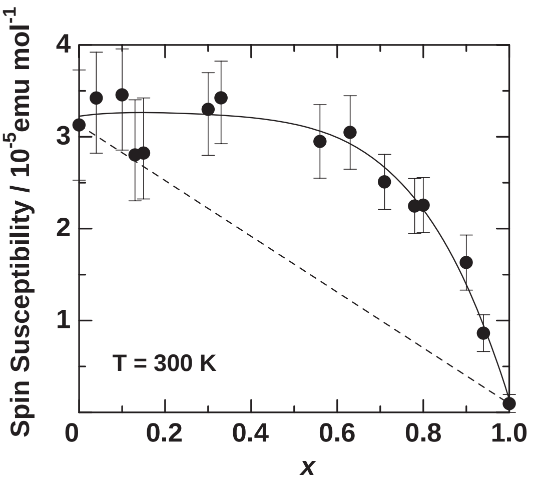

Fig. 8. Spin susceptibility of polycrystalline $[Ni_{1-x}Pd_x(chxn)_2Br]Br_2$ at room temperature. The dashed line shows the linear summation of the susceptibilities of the Ni and Pd fraction of pure cases. The solid curve is a guide for eyes.

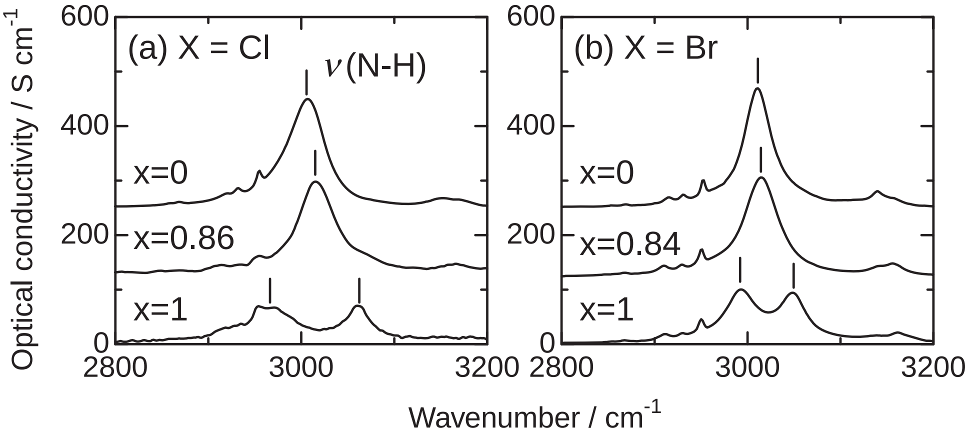

Fig. 7. The $\sigma$ spectra for IR region ($E_i$ // $a$ axis). The $\nu$(N–H) denotes the N–H stretching mode of chxn ligand.

order (Fig. 6). Therefore, the frequency of the peaks is sensitive to $\rho$. IR spectra of $[Ni_{1-x}Pd_x(chxn)_2X]X_2$ were measured using single-crystals.[14] As shown in Fig. 7, in the pure Ni compounds, a single $\nu$(N–H) band is observed at around 3000 cm$^{-1}$, reflecting the averaged valence ($Ni^{III}$) state. In the pure Pd compound, the $\nu$(N–H) band splits into two bands due to the formation of the mixed-valence ($Pd^{II}$ and $Pd^{IV}$) state. In the mixed-metal compounds, this splitting is observed when $x$ values exceed the critical value $x_c = 0.90$ for Br and 0.85 for Cl of the Pd concentration. This indicates that the oxidation state of the Pd ions with $x < x_c$ is the $Pd^{III}$ MH state, while that with $x > x_c$ is the $Pd^{II}$–$Pd^{IV}$ mixed-valence state or CDW state. On the other hand, in all range of $x$ values, the oxidation states of Ni ions are $Ni^{III}$ state. Therefore, the Pd ions undergo crossover from $Pd^{III}$ MH state to $Pd^{II}$–$Pd^{IV}$ mixed-valence states around $x_c$. The $x_c$ of the Cl compounds is smaller than that of the Br compounds, because the S of the Cl compounds is stronger than that of the Br compounds, and thus, the stability of the $Pd^{II}$–$Pd^{IV}$ mixed-valence state or CDW state of the Cl compounds is larger than that of the Br compounds.

## 5. ESR Spectra of $[Ni_{1-x}Pd_x(chxn)_2X]X_2$

Temperature dependence of the spin susceptibility $\chi$ of the $[Ni_{1-x}Pd_x(chxn)_2X]X_2$ showed Curie-like behavior at very low temperature, while weakly temperature dependent behaviors for high temperatures for all $x$ values are observed. The results for $x = 0$ and $x = 1$, that is, pure Ni and pure Pd complexes, were consistent with those reported by Okamoto et al.[10] In the pure Ni compound, the weakly temperature dependent $\chi$ for higher temperature is interpreted as a Bonner–Fisher type susceptibility of Heisenberg antiferromagnetic chain with $J \approx -2800$ K. Figure 8 shows the dependence of $\chi$ at room temperature on the mixing ratio for all values of $x$. As seen from the Fig. 8, $\chi$ retains nearly the same magnitude as $x$ increases from $x = 0$, which is the pure Ni case, to around $x \approx 0.5$, then it gradually drops to the values of $x = 1$, pure Pd case.[15] This shows that the $\chi$ exhibits a clear enhancement from the linear summation of the susceptibilities of antiferromagnetic Ni species and diamagnetic Pd species, which is shown by a dotted line in Fig. 8. Since the $\chi$ at the higher temperature should reflect the intrinsic magnetic property of the

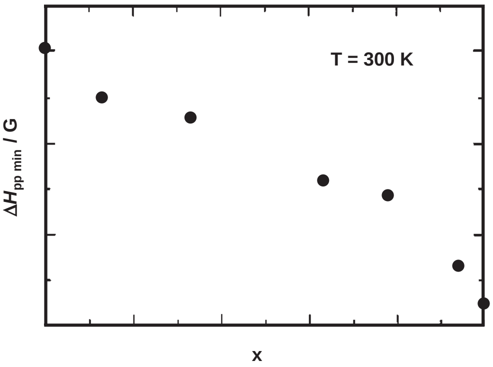

Fig. 9. The linewidth $\Delta H_{\mathrm{pp\,min}}$ at room temperature in $[\mathrm{Ni}_{1-x}\mathrm{Pd}_x(\mathrm{chxn})_2\mathrm{Br}]\mathrm{Br}_2$.

chains, the observed enhancement indicates that the magnetic states of the mixed-metal chains are significantly modified as compared with those of the pure Ni and Pd species. Generally speaking, the enhancement may occur due to two possibilities. The first possibility is that the enhanced fraction is due to the induced moments, $\mathrm{Pd^{III}}$ in Pd regions, which may be agree with the result of IR spectra mentioned above. The second possibility may be due to the introduction of non-magnetic $\mathrm{Pd^{II}}$–$\mathrm{Pd^{IV}}$ portions. This would cause a scission in the chains, which may more or less result in the reduction in the magnitude of exchange coupling. If this happens, the susceptibility should increase due to the suppression of antiferromagnetic spin correlation at a given temperature. The latter possibility, however, may be excluded for the following reasons. Figure 9 shows the dependence of the peak-to-peak ESR width at room temperature on the mixing ratio. In this case, the linewidth nearly linearly decreases as $x$ increases from Ni side to Pd side. A similar tendency was observed in temperature regions above 150 K. The observed behavior is clearly different from what is expected for a non-magnetic impurity effect on antiferromagnetic chains, at least for Ni-rich side. Since the linewidth of the Ni chains is determined by the exchange-narrowed width of antiferromagnetic chain, the introduction of a nonmagnetic impurity should result in the broadening of the linewidth due to the suppression of exchange narrowing. This is contrary to the observation. Moreover, the introduction of a nonmagnetic impurity is expected to increase the Curie spins at low temperature, which is not the case, either. Thus, the present results strongly suggest the first possibility of an induced moment due to $\mathrm{Pd^{III}}$ sites. Induced $\mathrm{Pd^{III}}$ spins are not isolated, and they may be interacting rather strongly to give the weak temperature dependent spin susceptibility close to those of antiferromagnetic Ni chains at higher temperatures, as observed.

Figure 10 shows the concentration dependence of the first derivative ESR spectra of $[\mathrm{Ni}_{1-x}\mathrm{Pd}_x(\mathrm{chxn})_2\mathrm{Br}]\mathrm{Br}_2$ single crystals against an external magnetic field $\boldsymbol{H}$ perpendicular to the $b$-axis at room temperature. Here, the sharp ESR spectrum obtained for $[\mathrm{Pd}(\mathrm{chxn})_2\mathrm{Br}]\mathrm{Br}_2$ ($x = 1$) is attributed to the thermally excited solitons, which were reported by Okamoto et al. From these spectra, $g$-values and peak-to-peak ESR linewidth $\Delta H_{\mathrm{pp}}$ are obtained as defined in Fig. 10. Both the $g$-values and corresponding $\Delta H_{\mathrm{pp}}$ are angular dependent at room temperature as shown in Fig. 11. Here, $\boldsymbol{H}$ is in the $ac$-plane for (a) and (c) and in the plane containing $b$-axis (hereafter called $b_{\parallel}$-plane) for (b) and (d). The angle $\theta$ in the $b_{\parallel}$-plane corresponds to the angle between $\boldsymbol{H}$ and $b$-axis, and $\varphi$ in the $ac$-plane are adjusted to 90° for one of the principal axes of the $g$-values. The $\Delta H_{\mathrm{pp}}$ shows the large angular dependence in both planes for $x < 0.94$. In contrast to $\Delta H_{\mathrm{pp}}$, nearly uniaxial anisotropy of $g$-values ($g_{\perp} > g_{\parallel} \approx 2$) are observed around the $b$-axis with a slight deviation in the $ac$-plane, where the deviation becomes larger as $x$ increases as discussed below. Observed principal $g$-values indicate that the unpaired electron resides on the $\mathrm{d}_{z^2}$ orbital of the metal ions, which are placed in a nearly tetragonal crystal field consisting of four N atoms of the two chxn ligands and the two bridging $\mathrm{Br}^-$ ions.

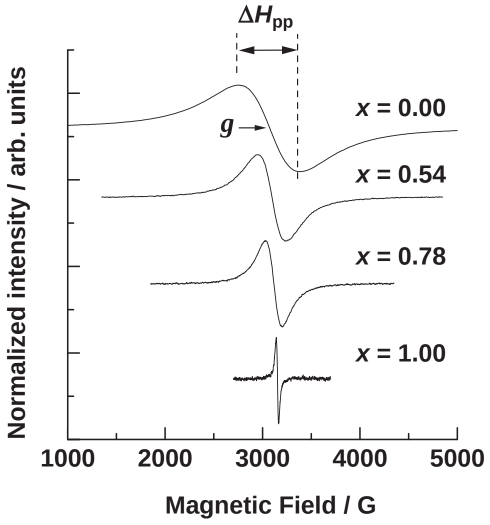

Fig. 10. First derivative ESR spectra of single-crystal $[\mathrm{Ni}_{1-x}\mathrm{Pd}_x(\mathrm{chxn})_2\mathrm{Br}]\mathrm{Br}_2$ at room temperature. The external magnetic field $\boldsymbol{H}$ is perpendicular to the chain direction ($b$-axis). The spectral intensities are normalized with their peak-to-peak height. The $g$-values and peak-to-peak ESR linewidth are obtained as defined in the figure.

As already mentioned, experimentally obtained $g$-values have a small anisotropy in the $ac$-plane, which implies that there is a small orthorhombic distortion of ligand molecules in these materials. Thus in the following discussion, we use the principal $g$-values $g_{\mathrm{max}}$ defined in Fig. 11a. By using this definition, we discuss the $x$-dependence of the $g$-value. In Fig. 12a, the $g_{\mathrm{max}}$ values obtained at room temperature and 10 K are plotted as crosses and solid circles, respectively. The $g_{\mathrm{max}}$-values show almost temperature independent behaviors and monotonically decrease as $x$ increases. This monotonic decrease in the $g_{\mathrm{max}}$ indicates the conversion of $\mathrm{Pd^{II}}$–$\mathrm{Pd^{IV}}$ (CDW) state into $\mathrm{Pd^{III}}$ states in the mixed-metal complexes. As already mentioned, the strong exchange interaction between $\mathrm{Ni^{III}}$ and $\mathrm{Pd^{III}}$ ions causes averaging of the two ESR lines into a single amalgamated line. In this case, the $g$-value for the mixed crystal is described by the weighted average equation as follows:

$$g^{\mathrm{Ni\text{–}Pd}}{}_{\mathrm{max}} = \frac{\chi_{\mathrm{Ni}}\cdot g^{\mathrm{Ni}}{}_{\mathrm{max}} + \chi_{\mathrm{Pd}}\cdot g^{\mathrm{Pd}}{}_{\mathrm{max}}}{\chi_{\mathrm{Ni}} + \chi_{\mathrm{Pd}}}, \qquad (1)$$

where $\chi_{\mathrm{Ni}}$ and $\chi_{\mathrm{Pd}}$ represent the contribution to the overall

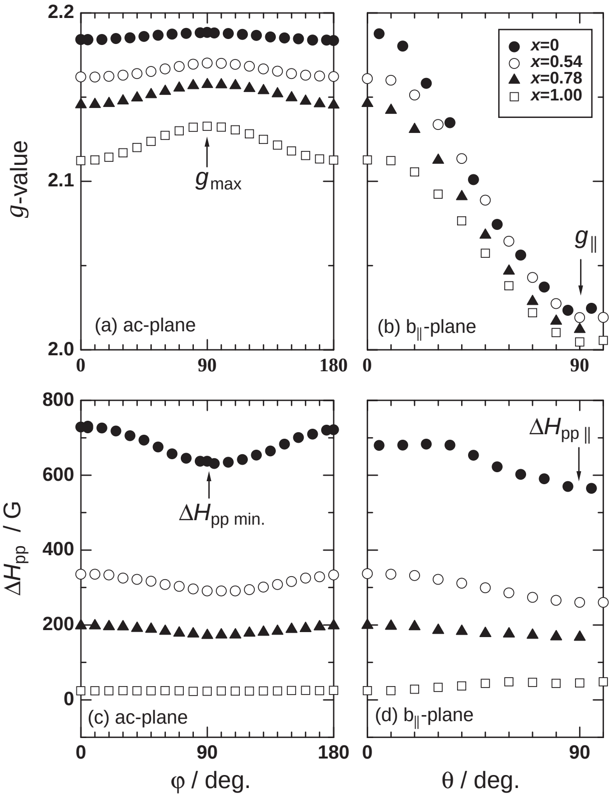

Fig. 11. Angular dependence of the $g$-value and corresponding linewidth $\Delta H_{\mathrm{pp}}$ at room temperature. (a) $g$-Values obtained with the external magnetic field $\boldsymbol{H}$ in the $ac$-plane, (b) $g$-values in the plane corresponding $b$-axis ($b_{\parallel}$-plane), (c) $\Delta H_{\mathrm{pp}}$ in the $ac$-plane, and (d) $\Delta H_{\mathrm{pp}}$ in the $b_{\parallel}$-plane corresponds to the angle between $\boldsymbol{H}$ and $b$-axis in the $b_{\parallel}$-plane, and $\varphi$ is adjusted to 90° for the principal axis of $g$-value in the $ac$-plane. The $g_{\mathrm{max}}$ and $g_{\parallel}$ show the principal $g$-values, and $\Delta H_{\mathrm{pp\,min}}$ and $\Delta H_{\mathrm{pp}\,\parallel}$ are their corresponding ESR linewidth, respectively.

magnetization from each paramagnetic species ($\mathrm{Ni^{III}}$ and $\mathrm{Pd^{III}}$) in the chain. Thus, the observed monotonic decrease of $g_{\mathrm{max}}$ in the mixed-metal complexes suggested that there is finite contribution from $\chi_{\mathrm{Pd}}$, namely, $\mathrm{Pd^{III}}$ ions which have smaller $g_{\mathrm{max}}$-value than that of $\mathrm{Ni^{III}}$ ions. Actually, the fraction of $\chi_{\mathrm{Pd}}$ greatly increases from $2.7 \times 10^{-7}$ emu mol$^{-1}$ for $\mathrm{[Pd(chxn)_2Br]Br_2}$ to $1.4 \times 10^{-5}$ emu mol$^{-1}$ for $x = 0.78$ at 280 K by using experimentally obtained spin susceptibility and $g$-values in Eq. 1 under the assumption that both $g^{\mathrm{Ni}}{}_{\mathrm{max}}$ and $g^{\mathrm{Pd}}{}_{\mathrm{max}}$ themselves are unchanged in the mixed-metal chain. This result shows excellent agreement with the previously obtained spin susceptibility enhancement. Figure 12a also shows that only 6% mixing of $\mathrm{Ni^{III}}$ ions drastically changes the oxidation state of the Pd ions. This result suggests that the strong U greatly affects the electronic states of these materials rather than S, which agree well with the theoretical expectation by Iwano.[16]

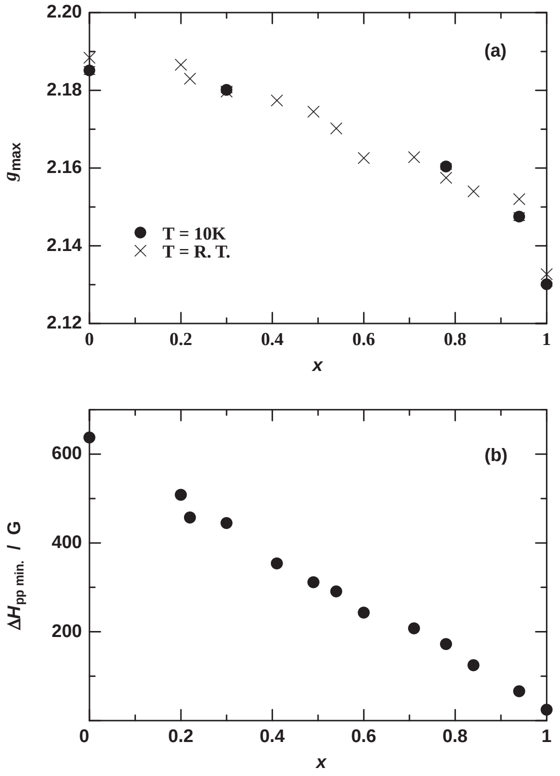

Fig. 12. The principal $g$-values $g_{\mathrm{max}}$ at 10 K (solid line) and room temperature (cross).

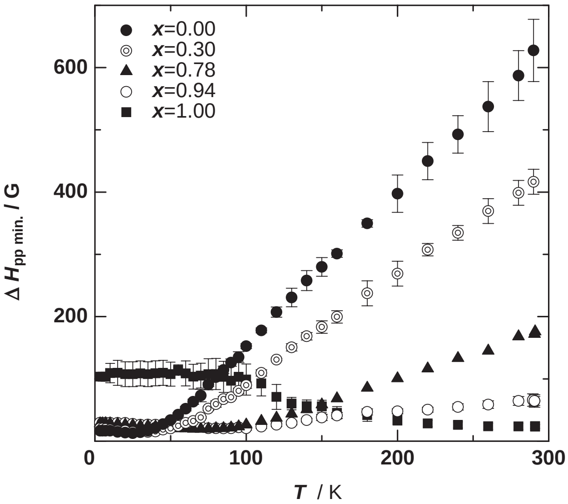

Fig. 13. Temperature dependence of $\Delta H_{\mathrm{pp\,min}}$.

In addition to the monotonic decrease of $g_{\mathrm{max}}$-value, the ESR linewidth $\Delta H_{\mathrm{pp}}$ also shows clear $x$-dependence. In contrast to the $g$-value, it shows large angular dependence both in the $ac$- and $b_{\parallel}$-plane as shown in Figs. 11c and 11d. The $x$-dependence of the values in the $ac$-plane, $\Delta H_{\mathrm{pp\,min}}$, defined in Fig. 11c are plotted in Fig. 12b. The monotonic decrease in $\Delta H_{\mathrm{pp\,min}}$ is also observed as $x$ increase. This decreasing $\Delta H_{\mathrm{pp\,min}}$ also provides evidence for the induced $\mathrm{Pd^{III}}$ ions in this systems. Before proceeding to further discussion, should be mentioned the origin of the $\Delta H_{\mathrm{pp}}$ in the case of pure Pd compound. In Fig. 13, we show the temperature dependence of $\Delta H_{\mathrm{pp\,min}}$. The line sharpening at temperatures higher than 100 K for $\mathrm{[Pd(chxn)_2Br]Br_2}$ is attributable to the motional narrowing of the thermally excited solitons in this material. In contrast to $\mathrm{[Pd(chxn)_2Br]Br_2}$, a small fraction of Ni drastically changes the temperature dependence of $\Delta H_{\mathrm{pp\,min}}$, i.e., gradual narrowing occurs as the temperature increases in the low-temperature region ($T < 50\,\mathrm{K}$) and then broadens but not for the pure Pd compound as shown in Fig. 13. Since the ESR spectra in the low-temperature region are dominated by the Curie component, which is of no importance in the present discussion of intrinsic magnetic properties, we use the room temperature $g$-value and $\Delta H_{\mathrm{pp}}$ shown in Figs. 11 and 12 in the following discussion.

To explain the origin of the high-temperature linewidth, the exchange-narrowed dipolar width $H_{\mathrm{d}}^2/H_{\mathrm{ex}}$ is excluded because it is estimated to be on the order of $10^{-2}\,\mathrm{G}$, using the dipolar width $H_{\mathrm{d}}$ of several hundred gauss, which was obtained from the lattice parameters and the exchange field $H_{\mathrm{ex}}$ of $1.9 \times 10^7\,\mathrm{G}$ with $J = 2800\,\mathrm{K}$ for $[\mathrm{Ni(chxn)_2Br}]\mathrm{Br_2}$. This value is much smaller than the observed value even when the exchange narrowing of the antiferromagnetic chain may give a width broader than $H_{\mathrm{d}}^2/H_{\mathrm{ex}}$ due to 1D spin diffusion.

The rather large temperature dependence of the linewidth of the pure Ni compound is consistent with that previously reported by Okamoto et al., who assigned the origin of the large temperature dependence of the linewidth to the spin-lattice relaxation time due to spin–orbit coupling, that is, the modulation of crystal field. Herein, we make a more detailed discussion of this mechanism based on the observed behavior of $\Delta H_{\mathrm{pp}}$. It is known that the relaxation rate of a direct process (one-phonon process), $1/T_{1\mathrm{D}}$, for a Kramers doublet is generally formalized as

$$\frac{1}{T_{1\mathrm{D}}} = \alpha\nu^2 T\cdot\left|\langle\psi'_-|\sum V_l|\psi'_+\rangle\right|^2, \qquad (2)$$

where $\nu$ is the microwave (or phonon) frequency, $\Sigma V_l$ is the crystalline field gradient associated with the $l$th normal mode of vibration of the ligands, and $|\Psi'_+\rangle$, $|\Psi'_-\rangle$ are the ground state wave functions taking into account of Zeeman interaction. $\alpha$ is a constant which contains the lattice information such as crystal density and sound velocity. This equation gives a linear temperature dependence for the linewidth, $\Delta H_{\mathrm{pp}} \propto 1/T_{1\mathrm{D}}$, which is consistent with the observation in Fig. 13. However, the small $\Delta H_{\mathrm{pp}}$ with motional narrowing effect observed for $[\mathrm{Pd(chxn)_2Br}]\mathrm{Br_2}$ suggests that $1/T_{1\mathrm{D}}$ for $\mathrm{Pd^{III}}$ ion is much smaller than that of $\mathrm{Ni^{III}}$ ion in this system. This difference in $1/T_{1\mathrm{D}}$ by substituting the metal ions from $\mathrm{Ni^{III}}$ to $\mathrm{Pd^{III}}$ is attributed to the modification of certain parameters, such as local phonon spectrum ($\alpha$), crystal field splitting energy, etc. in Eq. 2.

As shown in Figs. 11c and 11d, $\Delta H_{\mathrm{pp}}$ is anisotropic both in the *ac*- and $b_{\parallel}$-plane, which may be due to the contribution from various phonon modes $V_l$ in Eq. 2. However, roughly speaking, the systematic decrease in $\Delta H_{\mathrm{pp}}$ is observed in any direction as $x$ increases. Then, the comparison in the same principal axis in the *ac*-plane may allow us to discuss the $x$-dependence of $\Delta H_{\mathrm{pp\,min}}$ in this system qualitatively. As mentioned above, a rather small value of $1/T_{1\mathrm{D}}$ is expected for $\mathrm{Pd^{III}}$ ions, and it may be also true in the mixed-metal complexes. Then, the almost linear decrease in $\Delta H_{\mathrm{pp\,min}}$ in Fig. 12b suggests that $\mathrm{Pd^{III}}$ ions with a small linewidth are induced and contribute to the overall $\Delta H_{\mathrm{pp\,min}}$ in the form of some weighted average spectra with $\mathrm{Ni^{III}}$ ions, which have large linewidth. Such a consideration is consistent with a spin susceptibility enhancement and a decreasing $g$-value.

As a result, we have performed the single crystal ESR measurements of mixed-metal complexes $[\mathrm{Ni}_{1-x}\mathrm{Pd}_x(\mathrm{chxn})_2\mathrm{Br}]\mathrm{Br_2}$. Rapid suppression of the $\mathrm{Pd^{II}}$–$\mathrm{Pd^{IV}}$ (CDW) state is confirmed from the monotonic decrease in the principal $g$-values as $x$ increases, since decreasing $g$-values indicate the participation of magnetic $\mathrm{Pd^{III}}$ ion with a smaller $g$-value than that of $\mathrm{Ni^{III}}$ ion in the mixed-metal compounds. This result agrees with the observed susceptibility enhancement. From the obtained $g$-value, it is suggested that only 6% of the Ni concentration drastically affects the oxidation state of Pd ions. The peak-to-peak ESR linewidth $\Delta H_{\mathrm{pp}}$ also shows a monotonic decrease as $x$ increase, suggesting that there is a small contribution from induced $\mathrm{Pd^{III}}$ ions with smaller $\Delta H_{\mathrm{pp}}$ due to the longer spin-lattice relaxation time $T_{1\mathrm{D}}$. These results provide further evidence for the induced $\mathrm{Pd^{III}}$ spin moments in the present mixed-metal complexes.

## 6. Optical Conductivity Spectra of $[\mathrm{Ni}_{1-x}\mathrm{Pd}_x(\mathrm{chxn})_2\mathrm{X}]\mathrm{X}_2$

The optical conductivity spectra $\sigma$ of $[\mathrm{Ni}_{1-x}\mathrm{Pd}_x(\mathrm{chxn})_2\mathrm{X}]\mathrm{X}_2$ are shown in Fig. 14.[14] The pure Ni compound ($x = 0$) exhibits a prominent sharp peak (A) at around 1.8 eV for X = Cl and 1.3 eV for X = Br. This peak is attributed to the CT transition from X $\mathrm{p}_z$ to the upper-Hubbard band composed of $\mathrm{Ni^{III}}$ $\mathrm{d}_{z^2}$. With an increase $x$, the peak (A) broadens and another peak (B) appears on the lower energy side for both X = Cl and Br. For $x > 0.35$, peak (A) disappears, and peak (B) becomes dominant. With a further increase in $x$, peak (B) shifts to the lower energy, and when $x$ exceeds 0.9, peak (B) disappears,

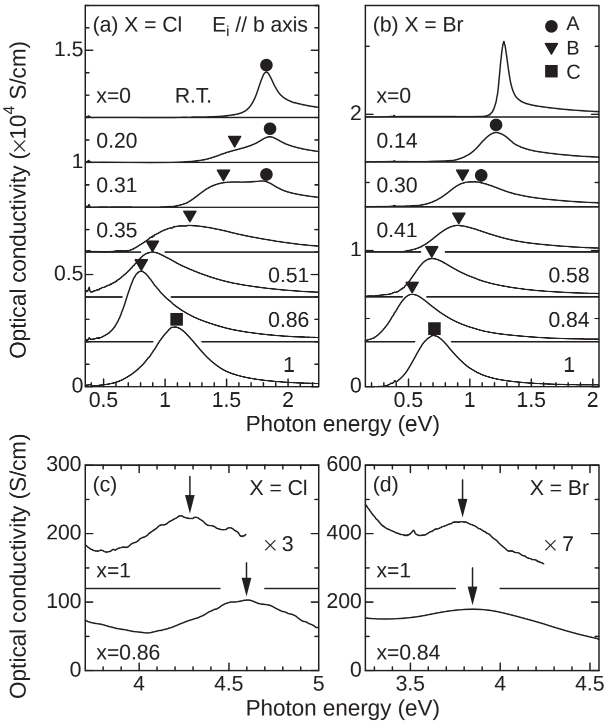

Fig. 14. The $\sigma$ spectra with the light polarization $E_i$ // $b$ axis (chain axis) at room temperature for (a) $[\mathrm{Ni}_{1-x}\mathrm{Pd}_x(\mathrm{chxn})_2\mathrm{Cl}]\mathrm{Cl_2}$, (b) $[\mathrm{Ni}_{1-x}\mathrm{Pd}_x(\mathrm{chxn})_2\mathrm{Br}]\mathrm{Br_2}$, (c) the X = Cl compounds ($x = 0.86$ and 1), and (d) the X = Br compounds ($x = 0.84$ and 1).

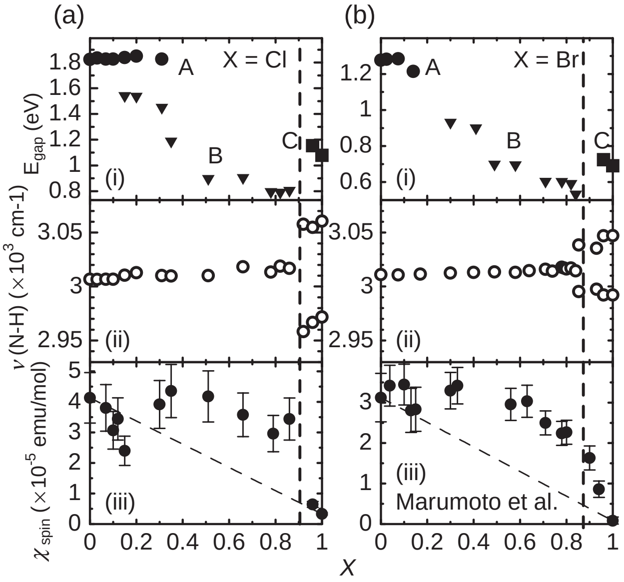

Fig. 15. (i) Energies of the peaks A–C, (ii) peak energies of $\nu$(N–H), and (iii) absolute magnitude of $\chi_{spin}$ at 300 K in (a) $[Ni_{1-x}Pd_x(chxn)_2Cl]Cl_2$, (b) $[Ni_{1-x}Pd_x(chxn)_2Br]Br_2$.

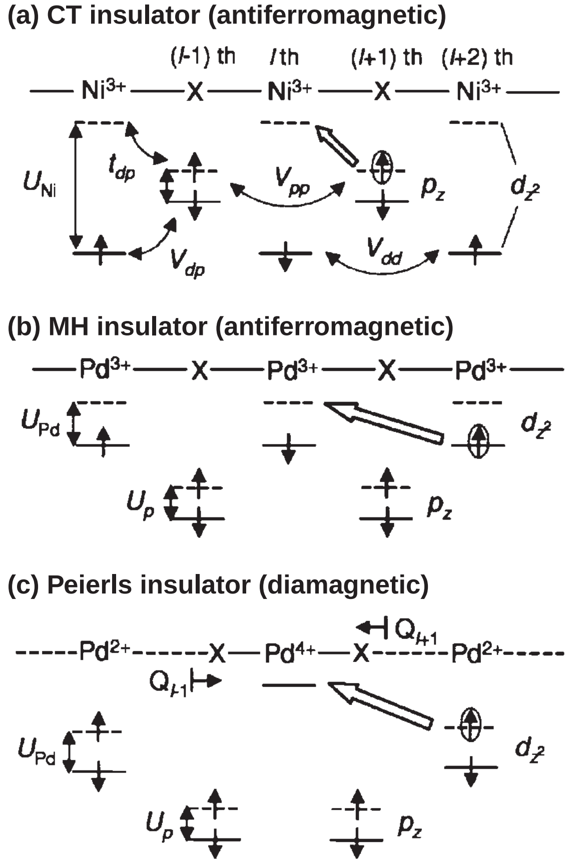

Fig. 16. Schematic electronic structures of (a) CT, (b) MH, and (c) Peierls insulator. Open arrows correspond to the lowest optical transition in each state.

and a higher energy peak (C) appears. The energy positions of peaks (A), (B), and (C) are plotted against $x$ in Figs. 15a and 15b. There is a discontinuous change in energy between peaks (B) and (C). The energy of peak (C) for $0.9 < x < 1$ is almost equal to that of the peak in the pure Pd compound ($x = 1$), which has been determined to be due to the inter-valence CT transition from the occupied $Pd^{II}$ $4d_{z^2}$ band to the unoccupied $Pd^{IV}$ $4d_{z^2}$ band, as shown in Fig. 16c.

For $x > x_c$, the system essentially represents a Peierls insulator, and the lowest optical transition (peak C) is attributed to the transition from $Pd^{II}$ to $Pd^{IV}$. For $x < x_c$, it is necessary to consider whether the system exists as a CT or MH insulator. The $\sigma$ spectra in the higher energy region (Figs. 14c and 14d) exhibit peak structures at around 4.5 eV for X = Cl ($x = 0.86$ and 1) and 4 eV for X = Br ($x = 0.84$ and 1). The structure in the pure Pd compounds can be assigned to the $X^- \rightarrow Pd^{IV}$ transition, which has been observed in the same energy region for the discrete $[X^-–Pd^{IV}–X^-]$ compound. A similar $X^- \rightarrow Pd^{IV}$ transition has been observed at around 5.1 and 4.8 eV for the Pd mixed-valence compounds with a CDW ground state $[Pd(en)_2][PdX_2(en)_2](ClO_4)_4$ with X = Cl and Br, respectively.[17] As the energy difference between the $X^- \rightarrow Pd^{IV}$ transition and $X^- \rightarrow Pd^{III}$ transition is expected not to be particularly large, the structure at around 4.5 eV in the Cl ($x = 0.86$) compound and 3.9 eV in the Br ($x = 0.84$) compound can be reasonably assigned to the $X^- \rightarrow Pd^{III}$ transitions. Therefore, peaks (B) at around 0.8 eV for X = Cl ($x = 0.86$) and 0.55 eV for X = Br ($x = 0.84$) are attributed to the $Pd^{III} \rightarrow Pd^{III}$ transitions shown in Fig. 16b. It is natural to consider that peak (B) at smaller $x$ represents a similar intermetallic transition, $Pd^{III} \rightarrow Pd^{III}$. As peak (A) is due to the $X^- \rightarrow Ni^{III}$ CT transition, the conversion from peak (A) to peak (B) observed at around $x \approx 0.3$ indicates the crossover from a CT insulator to a MH insulator. It should be noted that the introduction of a small amount excess of Ni sites (≈10–15%) renders the Peierls insulator unstable, and the system converts to a MH insulator, which is consistent with the observations from the IR and ESR spectra.

## 7. X-ray Diffuse Scattering of $[Ni_{1-x}Pd_x(chxn)_2Br]Br_2$

X-ray scattering experiments have been performed on the Ni–Pd mixed-metal complexes $[Ni_{1-x}Pd_x(chxn)_2Br]Br_2$.[18] Strong diffuse scattering was observed for $x > 0.7$, and it was interpreted as a special inhomogeneity in the valence of metal ions. This inhomogeneity takes the form of CDW, in which the metal ions within the chain alternate between +2 and +4. Correlations in the valence sequence were determined to be parallel as well as perpendicular to the chain direction. Pair correlation functions deduced from the measurements show the existence of a strong correlation between the positions of the bridging $Br^-$ ions and those of $Br^-$ counteranions. It is concluded that the valence of metal ions for $x < 0.7$ is +3. These results are almost consistent with the IR, ESR, and optical conductivity results.

## 8. Electrical Resistances of $[Ni_{1-x}Pd_x(chxn)_2Br]Br_2$

Figure 17a shows the hydrostatic pressure dependence of the electrical resistances along the crystallographic *ac*-plane of the mixed-metal complexes $[Ni_{1-x}Pd_x(chxn)_2Br]Br_2$ at room temperature.[19] The electrical resistance value is scaled with that at zero pressure for each $x$. The electrical resistance

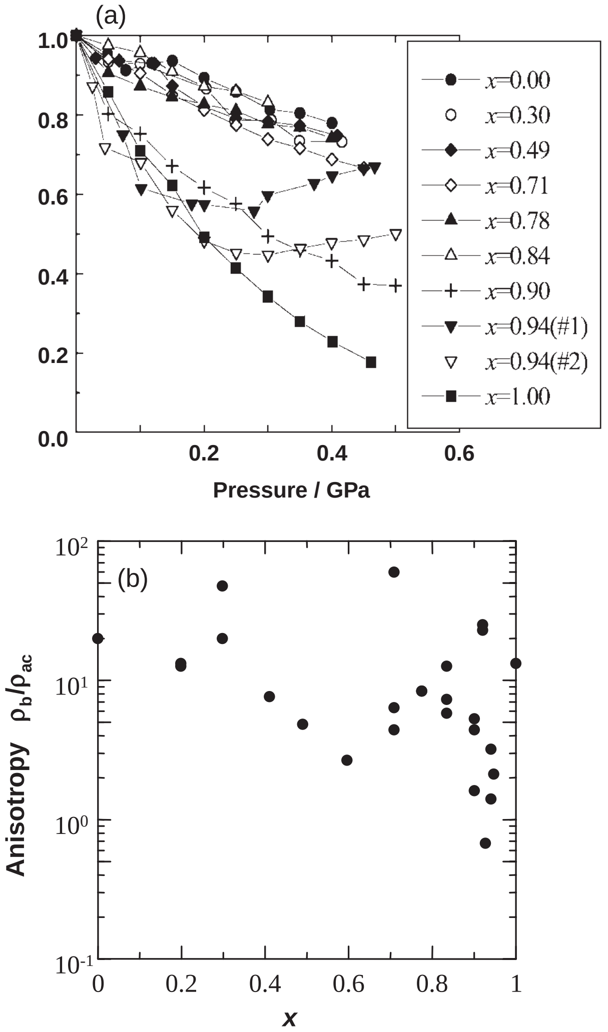

Fig. 17. Pressure dependence of the *ac*-plane resistance at room temperature (a), and the resistivity anisotropy at ambient pressure (b).

decrease under pressure is relatively small for $x = 0$ and large for $x = 1$. For $x < 0.84$, the electrical resistance decrease is as small as [Ni(chxn)$_2$Br]Br$_2$, as shown in Fig. 17a. At $x = 0.84$–$0.95$, intermediate behavior was found, suggesting that the crossover between MH and CDW states is around $x = 0.84$–$0.95$, in consistent with the other data.

Temperature dependence of the electrical resistance is semiconducting with activation energies of 0.08–0.16 eV, which agree with a previous report.[9] This value does not change significantly even at pressures up to 0.5 GPa. Using the Montgomery method, we evaluate the anisotropy in the electrical resistance. Figure 17b shows the anisotropy of the resistance at ambient pressure. In spite of the 1D chain structure, the anisotropy in the resistance is less than 50. At $x = 0.8$–$1$, the anisotropy is almost the order of unity. The anisotropy remains nearly the same under pressure or at $T > 120$ K. This suggests that conduction is not limited along the chain. Hopping among the chains occurs as frequently as those along the chain.

In Fig. 18, the thermopower of [Ni$_{1-x}$Pd$_x$(chxn)$_2$Br]Br$_2$ at room temperature (a) and at $T = 200$–$300$ K (b) are shown.

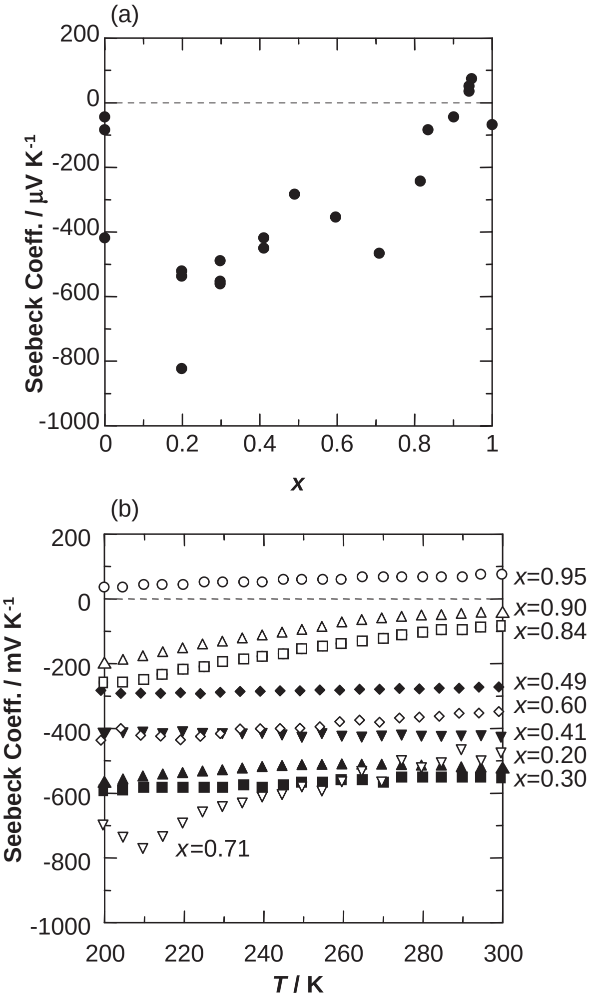

Fig. 18. Thermopower of the crystals at room temperature (a), and its temperature dependence at 200–300 K (b).

For $x = 0$ and $x = 1$, the temperature dependence could not be measured because the voltage readout was unstable due to high electrical resistance. Except for $x = 0.94$ and $0.95$, the thermopower indicates that the major carrier is negatively charged. For the sample with $x < 0.5$ (closed symbol in Fig. 18b), the thermopower is independent of temperature. The absolute value of the Seebeck coefficient |S| differs from sample to sample of the same $x$, however, an overall |S| increases with an increase in $x$. For the sample with $x > 0.6$, the thermopower shows semiconducting behavior (open symbols in Fig. 18b). For $x > 0.71$, |S| is reproducible among the samples with the same $x$ and decreases with an increase in $x$.

Figure 19 shows the activation energies determined from the resistance measurements and thermopower measurements for $x > 0.6$. The activation energies for the thermopower are smaller than that for the resistance measurement for $x = 0.8$–$0.9$.

For $x < 0.5$, the thermopower is independent of temperature. This suggests that the carriers are not thermally activated, but exist inherently in grown crystals. In the case of the hopping conduction of the small polarons, the temperature-independent thermopower is written as,

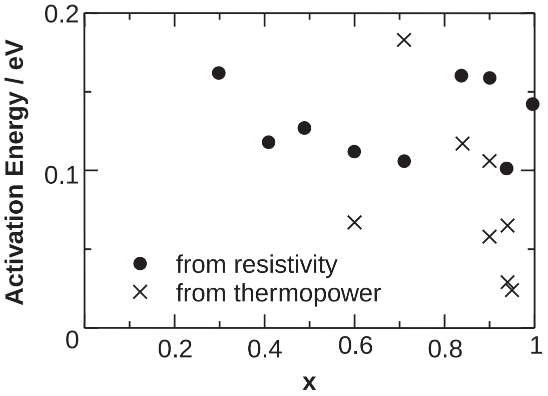

Fig. 19. The activation energy from resistance and thermopower measurements.

$$S = (k_B/e)\ln[N/n], \tag{3}$$

at enough high temperature, where $n$ is the carrier number, and $N$ is the possible hopping sites in the crystals. A typical value of $|S|$ ($500\,\mu V\,K^{-1}$) corresponds to $n/N = 0.003$. This value is on the same order as the Curie spin concentration of the present compounds found by ESR measurements. When $x < 0.5$, the nature of the charge carrier is similar to that in the $[Ni(chxn)_2Br]Br_2$, resulting in the same pressure dependence in the resistance as that at $x = 0$. In the present case, the $Ni^{II}$ or $Pd^{II}$ accompanied by halogen displacements forming small polarons are most probable negative carriers. The semiconducting behavior of the resistance is caused by the temperature-dependent hopping mobility.

For $x > 0.6$, the thermally activated carriers contribute to the conduction exhibiting semiconducting thermopower. It has been discussed that the thermal activation of the neutral solitons along the 1D chain contributes to the spin susceptibility and NMR relaxation in $[Pd(chxn)_2Br]Br_2$ with the activation energy of the order of 0.1 eV. In the Pd-rich compounds, the charge soliton-like excitations related to the $Pd^{II}$–$Pd^{IV}$ segments may be activated thermally and contribute to the conduction with the activation energy shown in Fig. 19. Some of them are negatively charged, but some of them may be positively charged in terms of the background charge neutrality. This causes the sign change in the thermopower at $x = 0.95$. Such carriers originate from the chains; however, they also hop among the chains resulting in the nearly isotropic transport. Under pressure, where metal–halogen bond alternation is suppressed, such segments may dissolve into independent carriers as in the case of the Ni-rich compounds.

The threshold concentration causing a large or intermediate pressure dependence in the electrical resistance and thermally activated thermopower is different; the former is $x = 0.84$ while the latter is $x = 0.6$. It is possible that the collective excitations are caused by the presence of the $Ni^{III}$ and do not contribute to the real electrical conduction up to $x = 0.8$.

From the pressure dependence of the resistance, the crossover between MH and CDW states is found to be between $x = 0.84$ and 0.95. Thermopower results imply that the charge carriers are small polarons localized at divalent metal ions for $x < 0.5$. For $x > 0.6$, thermally activated carriers contribute to the conduction.

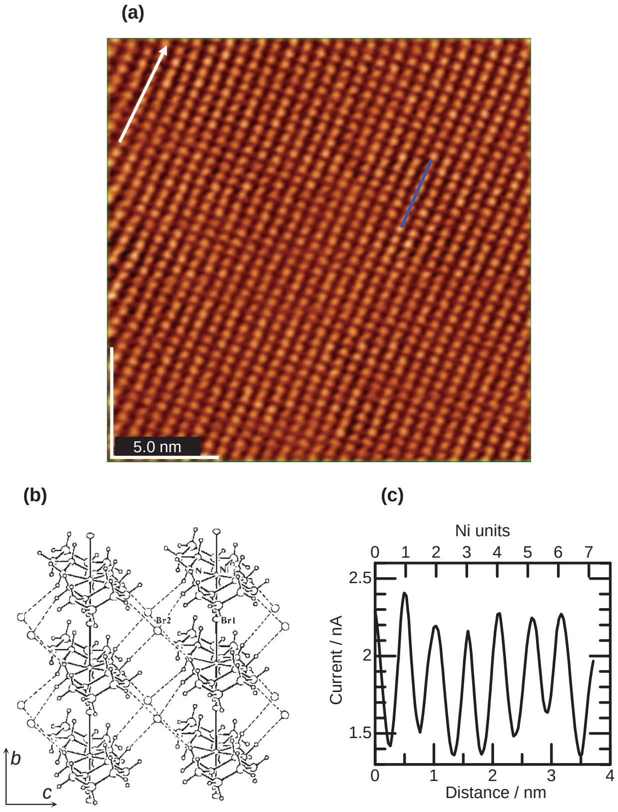

Fig. 20. a) STM image of $[Ni(chxn)_2Br]Br_2$ on the $bc$ plane (200 × 200 Å). The image was acquired with a sample bias of $V_s = +1.3$ V. The white arrow shows the 1D chain direction. b) Crystal structure of $[Ni(chxn)_2Br]Br_2$, c) Tunnel current profile of $[Ni(chxn)_2Br]Br_2$ on the blue line in Fig. 20a.

## 9. Direct Observation of Local Structure of $[Ni_{1-x}Pd_x(chxn)_2Br]Br_2$ by STM

STM is a powerful tool for studying local electronic structures in such compounds. Herein, we reported the first visualized local valence structures in Ni–Pd mixed-metal complexes obtained by STM.[20] STM measurements were performed at room temperature and under ambient pressure. Single-crystals of $[Ni_{1-x}Pd_x(chxn)_2Br]Br_2$ were cleaved and mounted on a sample stage with carbon paste so that the surface of the $bc$-plane could be observed. A positive sample bias voltage (Vs) was used.

Figure 20 shows an STM image of $[Ni(chxn)_2Br]Br_2$ in the range 200 × 200 Å. Bright spots in the image are observed every 5 × 7 Å. The crystal structure of $[Ni(chxn)_2Br]Br_2$ is shown in Fig. 20b. The Ni···Ni distances along the $b$ (1D chain) and $c$ axes are 5.16 and 7.12 Å, respectively, and hence, these spots reflect the periodicity of $[Ni(chxn)_2]$ units in the $bc$ plane. To investigate the valence structure in detail, we plotted a current profile along the 1D chain (on the blue line) in Fig. 20c. A maximum current is observed in every Ni unit, which indicates that all of the Ni centers are equivalent and in the CT insulator $Ni^{III}$–$Ni^{III}$ state in $[Ni(chxn)_2Br]Br_2$. This finding is consistent with the result obtained by single-crystal X-ray analysis.

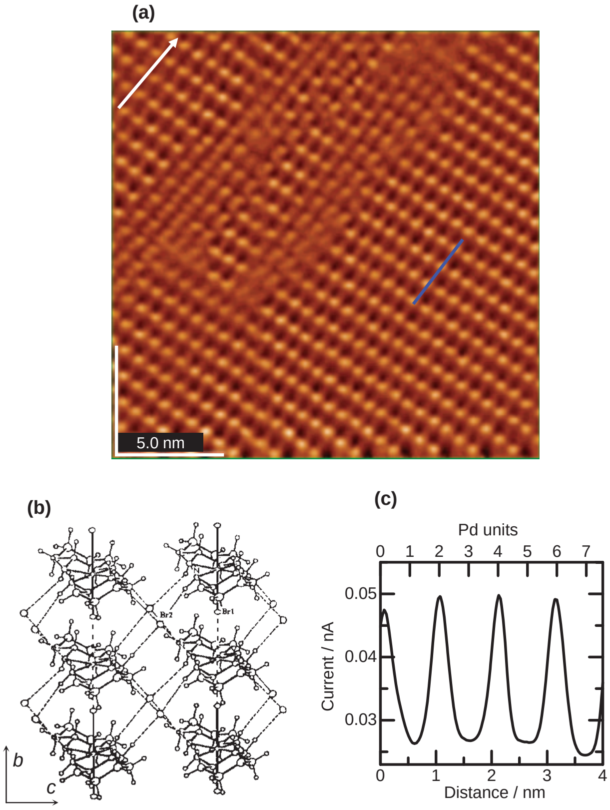

Fig. 21. a) STM image of $[Pd(chxn)_2Br]Br_2$ on the *bc* plane ($200 \times 200$ Å). The sample bias was $V_s = +1.0$ V. The 1D chain direction is shown by a white arrow. b) Crystal structure of $[Pd(chxn)_2Br]Br_2$. c) Current profile of $[Pd(chxn)_2Br]Br_2$ on the blue line in Fig. 21a.

An STM image in the range $200 \times 200$ Å and the crystal structure of $[Pd(chxn)_2Br]Br_2$ are shown in Figs. 21a and 21b, respectively. Bright spots are observed every $10 \times 7$ Å. The Pd···Pd distances along the *b* (1D chains) and *c* axes are 5.29 and 7.07 Å, respectively, and thus, these spots in the image reflect the twofold periodicity of the valence structure that result from the CDW structure of $[Pd(chxn)_2Br]Br_2$. The phase of the CDW is almost aligned in the *bc* plane, which is consistent with the X-ray diffusion scattering study, Therefore, correctly speaking, $[Pd(chxn)_2Br]Br_2$ should be formulated as $[Pd^{II}(chxn)_2][Pd^{IV}(chxn)_2Br_2]Br_4$.

Schematic band structures of $[Ni(chxn)_2Br]Br_2$ and $[Pd(chxn)_2Br]Br_2$ are shown in Fig. 22. Based on XPS and Auger spectroscopy, the $d_{z^2}$ band of Ni splits into the occupied lower-Hubbard band (LH) and unoccupied upper-Hubbard (UH) bands as a consequence of strong electron correlation and, as a result, the valence and conduction bands of $[Ni(chxn)_2Br]Br_2$ are the $p_z$ band of the bridging Br atoms and the UH band composed of the $d_{z^2}$ orbital of Ni ions, respectively. In $[Pd(chxn)_2Br]Br_2$, on the other hand, the valence and conduction bands are the $d_{z^2}$ bands of $Pd^{II}$ and $Pd^{IV}$, respectively. As the STM measurements were performed with a positive sample bias, the tunnel current is observed from a Fermi energy ($E_F$) of the tip to a conduction band of the sample. Therefore, in $[Ni(chxn)_2Br]Br_2$, the tunnel current from $E_F$ to the UH $d_{z^2}$ band of $Ni^{III}$ is observed, whereas that from $E_F$ to $d_{z^2}$ band of $Pd^{IV}$ is observed in $[Pd(chxn)_2Br]Br_2$, which affords the two-fold periodicity along the 1D chain observed in the STM image.

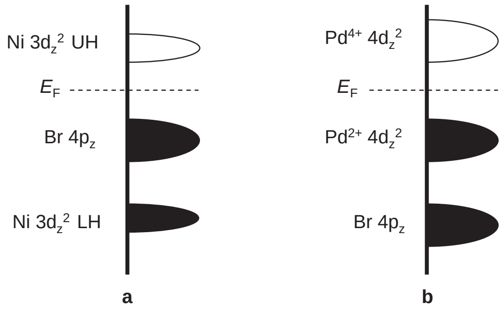

Fig. 22. Schematic band structure of a) $[Ni(chxn)_2Br]Br_2$ and b) $[Pd(chxn)_2Br]Br_2$.

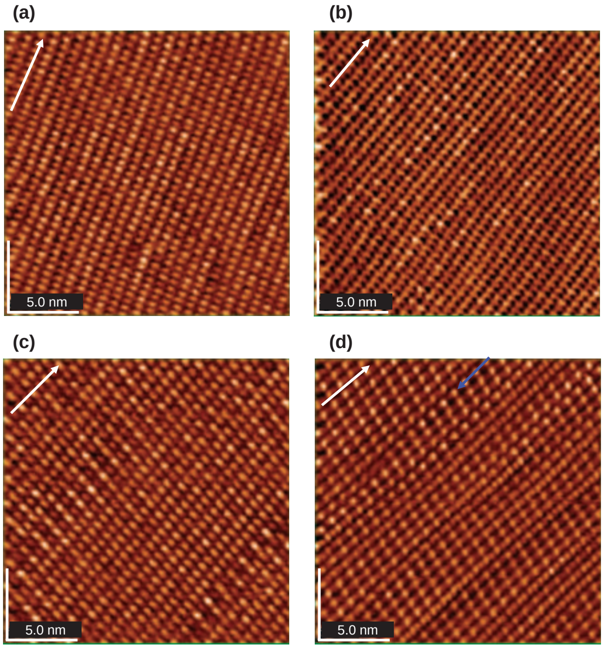

Fig. 23. STM images of $[Ni_{1-x}Pd_x(chxn)_2Br]Br_2$ with a) $x = 0.70$, b) $x = 0.80$, c) $x = 0.86$, and d) $x = 0.95$ on the *bc* plane ($200 \times 200$ Å). The sample bias was $V_s = +1.0$ V. The 1D chain directions are shown as white arrows; the blue arrow shows the 1D chain on which the spin soliton is observed.

Next, we carried out STM measurements on the mixed-metal complexes $[Ni_{1-x}Pd_x(chxn)_2Br]Br_2$ to determine their local valence structures. Figure 23 shows the STM images of the complexes with a) $x = 0.70$, b) $x = 0.80$, c) $x = 0.86$, and d) $x = 0.95$. in an area of $200 \times 200$ Å. In the $x = 0.70$ complex (Fig. 23a), an image similar to that of $[Ni(chxn)_2Br]Br_2$ is observed with almost no two-fold periodicity. This result shows that the $x = 0.70$ complex forms almost in the MH state, where the oxidation state of the Pd center is +3. In the $x = 0.80$ complex (Fig. 23b), on the other hand, two-fold periodicity is observed in several areas, which are attributed to the CDW states. This CDW state has coherence over approximately 10 metal sites along the *b*-axis, but almost no coherence along the *c*-axis. In the $x = 0.86$ complex (Fig. 23c), the CDW coherence

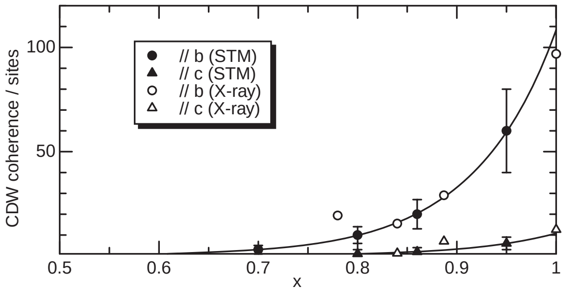

Fig. 24. CDW coherence as a function of $x$. The filled circle and triangle represent CDW coherence along the chain and $c$ axis, respectively, determined by STM measurement. The open circle and triangle represent those determined by X-ray diffuse scattering measurements. The solid lines are guides to the eyes.

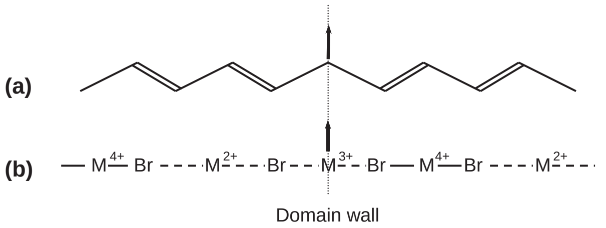

Fig. 25. Schematic chain structure of the spin soliton in a) *trans*-polyacetylene, and b) halogen-bridged CDW complexes.

is clearly more propagated than that in the $x = 0.80$ complex. In the $x = 0.86$ complex, the CDW coherence spreads over approximately 21 metal sites along the $b$ axis and 2 or 3 metal sites along the $c$ axis. Figure 23d shows the STM image of the $x = 0.95$ complex. A large part of this image has two-fold periodicity, that is, a CDW state. Along the $b$ axis, a large part of the chains with a CDW state conserve the two-fold periodicity within the measured length (ca. 40 metal sites), which shows that CDW coherence along the chain is longer than 20 nm. Along the $c$-axis, on the other hand, the CDW coherence spreads over approximately 6 or 7 sites. We plotted the CDW coherence length as a function of $x$ in Fig. 24 together with the data evaluated by X-ray diffuse scattering measurements reported by Wakabayashi et al.[18] The CDW coherence determined by STM measurements is in good agreement with the X-ray diffuse scattering results. It was revealed that the CDW coherence is propagated with increasing value of $x$.

In addition, the phase of the CDW in the chain, shown as a blue arrow in Fig. 23d, is reversed. This reversal is due to the generation of a soliton. A schematic chain structure with the spin soliton in a CDW complex is shown together with *trans*-polyacetylene (*trans*-PA) in Fig. 25. It is well known that the spin soliton in *trans*-PA is made by a domain wall originating from the mismatch of the phase of the alternating bonds. On the other hand, it has been shown that the spin solitons in CDW complexes are made by mismatch of the CDW phase, and $M^{III}$ site act as domain walls.[2a] This domain wall of the spin soliton observed in Fig. 23d spreads over approximately 10 metal sites, which is consistent with the theoretical prediction.[16] Although the mechanism of the spin soliton in the complex is the same as that in *trans*-PA, there is a marked difference in the activation energy for the soliton motion. This energy has been determined to be about 80 meV by using light-induced ESR studies,[21] which is much larger than that of *trans*-PA (2 meV).[22] Because the soliton motion in $[Pd(chxn)_2Br]Br_2$ is much slower than that of *trans*-PA, it can be observed by STM, which operates on the millisecond-order timescale. Although the spin solitons are well known in $\pi$-conjugated polymers,[23] this is the first time that the spin soliton has been obsreved in real space.

In summary, we have succeeded in synthesizing a series of single-crystals of $[Ni_{1-x}Pd_x(chxn)_2X]X_2$, where electron-correlation and electron–phonon interaction compete with each other. By use of IR, ESR, optical conductivities, X-ray diffusion scattering, and STM, we showed that while the oxidation state of the Ni ions is +3 for all $x$ ranges, the Pd ions undergo crossover from $Pd^{III}$ MH state to $Pd^{II}$–$Pd^{IV}$ mixed-valence states or CDW state around $x \approx 0.9$ for Br and $x \approx 0.85$ for Cl.

The authors acknowledge Dr. T. Manabe for his synthetic works of the Ni–Pd mixed-metal complexes. The authors are grateful to Prof. H. Okamoto, Prof. H. Kishida, and Dr. Matsuzaki at the University of Tokyo for their kind support in optical measurements and discussion. They are also grateful to Prof. S. Kuroda, Prof. H. Ito, Dr. K. Marumoto, and Dr. H. Tanaka at Nagoya University for their ESR and electrical conductivity measurements and discussion. The authors also acknowledge Dr. Y. Wakabayashi at KEK for X-ray diffusion scattering measurements. Finally the authors are grateful to Dr. T. Takami at Visionarts Research Inc., and Prof. K.-i. Sugiura and Prof. H. Miyasaka at Tokyo Metropolitan University for their kind help with the STM measurements and discussion.

This work was partly supported by a Grant-in-Aid for Creative Scientific Research from the Ministry of Education, Culture, Sports, Science and Technology.

## References

1 *Extended Linear Chain Compounds*, ed. by J. S. Miller, Plenum, New York and London, **1982**, Vols. I–III.

2 a) H. Okamoto, M. Yamashita, *Bull. Chem. Soc. Jpn.* **1998**, *71*, 2023. b) A. R. Bishop, B. I. Swanson, *Los Alamos Sci.* **1993**, *21*, 133. c) R. J. H. Clark, *Adv. Infrared Raman Spectrosc.* **1983**, *11*, 95. d) M. Yamashita, T. Manabe, T. Kawashima, H. Okamoto, H. Kitagawa, *Coord. Chem. Rev.* **1999**, *190–192*, 309. e) N. Kuroda, M. Nishida, M. Yamashita, *Phys. Rev. B* **1995**, *52*, 17084. f) N. Kuroda, M. Nishida, M. Yamashita, *Phys. Rev. B* **1996**, *54*, 2390. g) H. Okamoto, Y. Oka, T. Mitani, M. Yamashita, *Phys. Rev. B* **1997**, *55*, 6330. h) N. Kuroda, Y. Wakabayashi, M. Nishida, N. Wakabayashi, M. Yamashita, N. Matsushita, *Phys. Rev. Lett.* **1997**, *79*, 2510. i) H. Okamoto, Y. Kaga, Y. Shimizu, Y. Oka, Y. Iwasa, T. Mitani, M. Yamashita, *Phys. Rev. Lett.* **1998**, *80*, 861.

3 a) Y. Wada, K. Era, M. Yamashita, *Solid State Commun.* **1988**, *67*, 953. b) H. Ooi, M. Yamashita, T. Kobayashi, *Solid State Commun.* **1993**, *86*, 789. c) H. Ooi, M. Yamashita, T. Kobayashi, *Chem. Phys. Lett.* **1993**, *210*, 384. d) Y. Wada, U. Lemmer, E. O. Gobel, M. Yamashita, K. Toriumi, *Phys. Rev. B* **1995**, *52*, 8276. e) T. Kobayashi, T. Sekikawa, M. Yamashita, *Chem. Lett.* **1997**, 1029. f) A. Sugita, T. Saito, H. Kano, M. Yamashita, T. Kobayashi, *Phys. Rev. Lett.* **2001**, *86*, 2158.

4 H. Okamoto, T. Mitani, K. Toriumi, M. Yamashita, *Phys.*

*Rev. Lett.* **1992**, *69*, 2248.

5 a) Y. Iwasa, E. Funatsu, T. Koda, M. Yamashita, *Mol. Cryst. Liq. Cryst.* **1992**, *217*, 37. b) Y. Iwasa, E. Funatsu, T. Koda, M. Yamashita, *Appl. Phys. Lett.* **1991**, *59*, 2219.

6 a) H. Kishida, H. Matsuzaki, H. Okamoto, T. Manabe, M. Yamahsita, T. Taguchi, Y. Tokura, *Nature* **2000**, *405*, 929. b) H. Okamoto, H. Kishida, M. Ono, H. Matsuzaki, Y. Taguchi, Y. Tokura, M. Yamashita, *Nonlinear Opt.* **2002**, *29*, 687. c) M. Ono, K. Miura, A. Maeda, H. Matsuzaki, H. Kishida, Y. Taguchi, Y. Tokura, M. Yamashita, H. Okamoto, *Phys. Rev. B* **2004**, *70*, 85101.

7 a) K. Nasu, *J. Phys. Soc. Jpn.* **1983**, *52*, 3865. b) K. Nasu, *J. Phys. Soc. Jpn.* **1984**, *53*, 302. c) G. T. Gammel, A. Saxena, I. Bastistic, A. R. Bishop, S. R. Phillpot, *Phys. Rev. B* **1992**, *45*, 6408.

8 M. B. Robin, P. Day, *Adv. Inorg. Radiochem.* **1967**, *10*, 247.

9 a) H. Okamoto, T. Mitani, K. Toriumi, M. Yamashita, *Mater. Sci. Eng.* **1992**, *B13*, 9. b) M. Yamashita, D. Kawakami, S. Matsunaga, Y. Nakayama, M. Sasaki, S. Takaishi, F. Iwahori, H. Miyasaka, K. Sugiura, Y. Wada, H. Miyamae, H. Matsuzaki, H. Okamoto, H. Tanaka, K. Marumoto, S. Kuroda, *Angew. Chem., Int. Ed.* **2004**, *43*, 4763. c) M. Yamashita, Y. Nonaka, S. Kida, Y. Hamaue, R. Aoki, *Inorg. Chim. Acta* **1981**, *52*, 43. d) M. Yamashita, H. Ito, K. Toriumi, T. Ito, *Inorg. Chem.* **1983**, *22*, 1566. e) M. Yamashita, I. Murase, T. Ito, Y. Wada, T. Mitani, I. Ikemoto, *Bull. Chem. Soc. Jpn.* **1985**, *58*, 2336. f) R. J. H. Clark, D. J. Michael, M. Yamashita, *J. Chem. Soc., Dalton Trans.* **1991**, 725. g) R. J. H. Clark, D. J. Michael, M. Yamashita, *J. Chem. Soc., Dalton Trans.* **1991**, 3447. h) T. Kawashima, K. Takai, H. Aso, T. Manabe, K. Yakizawa, C. Kachi, T. Ishii, H. Miyasaka, H. Matsuzaka, M. Yamashita, H. Okamoto, H. Kitagawa, M. Shiro, K. Toriumi, *Inorg. Chem.* **2001**, *40*, 6651.

10 a) K. Toriumi, Y. Wada, T. Mitani, S. Bandow, M. Yamashita, Y. Fujii, *J. Am. Chem. Soc.* **1989**, *111*, 2341. b) K. Toriumi, H. Okamoto, T. Mitani, S. Bandow, M. Yamashita, Y. Wada, Y. Fujii, R. J. H. Clark, D. J. Michael, A. J. Edward, D. Watkin, M. Kurmoo, P. Day, *Mol. Cryst. Liq. Cryst.* **1990**, *181*, 333. c) H. Okamoto, K. Toriumi, T. Mitani, M. Yamashita, *Phys. Rev. B* **1990**, *42*, 10381. d) H. Okamoto, Y. Shimada, Y. Oka, A. Chainani, T. Takahashi, H. Kitagawa, T. Mitani, K. Toriumi, T. Manabe, M. Yamashita, *Phys. Rev. B* **1996**, *54*, 8438. e) S. Fujimori, A. Ino, T. Okane, A. Fujimori, K. Okada, T. Manabe, M. Yamashita, H. Kishida, H. Okamoto, *Phys. Rev. Lett.* **2002**, *88*, 247601. f) M. Yamashita, T. Manabe, K. Inoue, T. Kawashima, H. Okamoto, H. Kitagawa, T. Mitani, K. Toriumi, H. Miyamae, R. Ikeda, *Inorg. Chem.* **1999**, *38*, 1894.

11 S. Takaishi, Y. Tobu, H. Kitagawa, A. Goto, T. Shimizu, T. Okubo, T. Mitani, R. Ikeda, *J. Am. Chem. Soc.* **2004**, *126*, 1614.

12 M. Yamashita, T. Ishii, H. Matsuzaka, T. Manabe, T. Kawashima, H. Okamoto, H. Kitagawa, T. Mitani, K. Marumoto, S. Kuroda, *Inorg. Chem.* **1999**, *38*, 5124.

13 a) K. Okaniwa, H. Okamoto, T. Mitani, K. Toriumi, M. Yamashita, *J. Phys. Soc. Jpn.* **1991**, *60*, 997. b) H. Okamoto, K. Toriumi, K. Okaniwa, T. Mitani, M. Yamashita, *Synth. Met.* **1991**, *42*, 2791.

14 H. Matsuzaki, K. Iwano, T. Aizawa, M. Ono, H. Kishida, M. Yamashita, H. Okamoto, *Phys. Rev. B.* **2004**, *70*, 035204.

15 a) S. Kuroda, K. Marumoto, T. Manabe, M. Yamashita, *Synth. Met.* **1999**, *103*, 2155. b) H. Tanaka, K. Marumoto, S. Kuroda, T. Manabe, M. Yamashita, *Synth. Met.* **2001**, *120*, 949. c) H. Tanaka, K. Marumoto, S. Kuroda, T. Manabe, M. Yamashita, *J. Phys. Soc. Jpn.* **2002**, *71*, 1370.

16 K. Iwano, *J. Phys. Soc. Jpn.* **1999**, *68*, 935.

17 a) Y. Wada, T. Mitani, M. Yamashita, T. Koda, *J. Phys. Soc. Jpn.* **1985**, *54*, 3134. b) Y. Wada, T. Mitani, K. Toriumi, M. Yamashita, *J. Phys. Soc. Jpn.* **1989**, *58*, 3013.

18 Y. Wakabayashi, N. Wakabayashi, M. Yamashita, T. Manabe, N. Matsushita, *J. Phys. Soc. Jpn.* **1999**, *68*, 3948.

19 H. Ito, M. Sunata, S. Kuroda, T. Manabe, M. Yamashita, *Mol. Cryst. Liq. Cryst.* **2002**, *379*, 285.

20 a) S. Takaishi, H. Miyasaka, K. Sugiura, M. Yamashita, H. Matsuzaki, H. Kishida, H. Okamoto, H. Tanaka, K. Marumoto, H. Ito, S. Kuroda, T. Takami, *Angew. Chem., Int. Ed.* **2004**, *43*, 3171. b) M. Sasaki, S. Takaishi, H. Miyasaka, K. Sugiura, M. Yamashita, *J. Am. Chem. Soc.* **2005**, *43*, 14958.

21 H. Tanaka, K. Marumoto, S. Kuroda, M. Yamashita, *Synth. Met.* **2003**, *135–136*, 317.

22 B. R. Weinberger, E. Ehrenfreund, A. Pron, A. J. Heeger, A. G. MacDiarmid, *J. Chem. Phys.* **1980**, *72*, 4749.

23 a) I. B. Goldberg, H. R. Crwe, P. R. Newman, A. J. Heeger, A. G. MacDiarmid, *J. Chem. Phys.* **1979**, *70*, 1132. b) W. P. Su, J. R. Schrieffer, A. J. Heeger, *Phys. Rev. B* **1980**, *22*, 2099.

Award recipient

Masahiro Yamashita was born in 1954 in Karatsu in Saga, Japan. He received his B.Sc. Degree in 1977, M.Sc. in 1979, and D.Sc. in 1982 from Kyushu University, working under the supervision of Prof. S. Kida. After his graduation, he joined the Institute for Molecular Science. In 1985, he was appointed as assistant Professor at Kyushu University. In 1989, he was appointed as associate professor at Nagoya University, and he was promoted as a full professor in the same university in 1998. He was a full professor at Tokyo Metropolitan University from 2000 to 2004. He is now a full professor of Department of Chemistry in Tohoku University. He is also working on Core Research for Evolutional Science and Technology (CREST) project in Japan Science and Technology Corporation (JST). He has been honored with the Inoue Scientific Award (2002), and The Chemical Society of Japan Award for Creative Work (2004). His current interests include the multi-functional nano-science of advanced metal complexes.

Shinya Takaishi was born in 1975 in Ube in Yamaguchi, Japan. He received his B.Sc. Degree in 1998, M.Sc. in 2000, and D.Sc. in 2003 from The University of Tsukuba, working under the supervision of Prof. R. Ikeda. After his graduation, he joined the Tokyo Metropolitan University. In 2004, he was appointed as assistant Professor at Tohoku University. His current interests include the novel quantum phenomena in the low-dimensional molecular system.